JGP Journal of General Physiology

ARTICLE

Mechanistic understanding of KCNQ1 activating polyunsaturated fatty acid analogs

Jessica J. Jowais[1*], Samira Yazdi[2*], Alessia Golluscio[1], Vanessa Olivier-Meo[1], Sara I. Liin[2], and H. Peter Larsson[1]

The KCNQ1 channel is important for the repolarization phase of the cardiac action potential. Loss of function mutations in KCNQ1 can cause long QT syndrome (LQTS), which can lead to cardiac arrythmia and even sudden cardiac death. We have previously shown that polyunsaturated fatty acids (PUFAs) and PUFA analogs can activate the cardiac KCNQ1 channel, making them potential therapeutics for the treatment of LQTS. PUFAs bind to KCNQ1 at two different binding sites: one at the voltage sensor (Site I) and one at the pore (Site II). PUFA interaction at Site I shifts the voltage dependence of the channel to the left, while interaction at Site II increases maximal conductance. The PUFA analogs, linoleic–glycine and linoleic–tyrosine, are more effective than linoleic acid at Site I, but less effective at Site II. Using both simulations and experiments, we find that the larger head groups of linoleic–glycine and linoleic–tyrosine interact with more residues than the smaller linoleic acid at Site I. We propose that this will stabilize the negatively charged PUFA head group in a position to better interact electrostatically with the positively charges in the voltage sensor. In contrast, the larger head groups of linoleic–glycine and linoleic–tyrosine compared with linoleic acid prevent a close fit of these PUFA analogs in Site II, which is more confined. In addition, we identify several KCNQ1 residues as critical PUFA-analog binding residues, thereby providing molecular models of specific interactions between PUFA analogs and KCNQ1. These interactions will aid in future drug development based on PUFA–KCNQ1 channel interactions.

Introduction

The cardiac KCNQ1 channel together with the β subunit KCNE1 is responsible for one of the dominant repolarizing currents of the ventricular action potential, known as the slow delayed-rectifier potassium current (IKs; Barhanin et al., 1996; Salata et al., 1996; Sanguinetti et al., 1996). Loss-of-function mutations in the KCNQ1 channel reduce the IKs current, which can prolong the ventricular action potential and cause long QT syndrome type 1 (LQT1; Alders et al., 1993; Bohnen et al., 2017). LQT1 is an arrhythmogenic disorder that can cause torsades de pointes, ventricular fibrillation, and sudden cardiac death (Bohnen et al., 2017). Current treatments for LQT1 syndrome include β blockers and implantation of a cardioverter defibrillator (Cho, 2016; Schwartz et al., 2012; Waddell-Smith and Skinner, 2016). They are largely effective in treating most patients, but they do not work for all individuals (Chockalingam et al., 2012; Schwartz et al., 2012). We have shown previously that polyunsaturated fatty acids (PUFAs) can activate the KCNQ1/KCNE1 channel, thereby increasing the IKs current (Liin et al., 2015). This effect has been shown to shorten the action potential duration in human cardiomyocytes, illustrating PUFA's potential as a new therapeutic for LQT1 (Bohannon et al., 2020a). For this reason, we are interested in better understanding the molecular mechanisms behind PUFAs effects on the KCNQ1 channel to aid in the possible development of PUFA-based LQT1 drugs.

A cryo-EM structure of the *Xenopus laevis* KCNQ1 (xKCNQ1) and human KCNQ1 (hKCNQ1) channel has been published, giving details about the KCNQ1 structure and a molecular model (Sun and MacKinnon, 2017, 2020). KCNQ1 has six transmembrane segments contained (S1–S6) in each subunit (Fig. 1, A and B). Four subunits come together to form a tetrameric voltage-gated potassium channel. S1–S4 in each subunit make up the voltage-sensing domain of the channel with positively charged arginine residues on S4 acting as the voltage sensor (Fig. 1, A and B). When a cell depolarizes, the voltage sensors move outward and trigger the opening of the channel allowing for outward flux of potassium (Barro-Soria et al., 2014; Hou et al., 2017; Westhoff et al., 2019). The pore domain and potassium selectivity filter are formed by S5–S6 from all four subunits (Fig. 1, A and B).

We have shown that PUFAs activate the KCNQ1 channel in two ways: they shift the voltage dependence of channel opening

[1]Department of Physiology and Biophysics, University of Miami, Miami, FL, USA; [2]Department of Biomedical and Clinical Sciences, Linköping University, Linköping, Sweden.

Correspondence to H. Peter Larsson: plarsson@med.miami.edu; Sara I. Liin: sara.liin@liu.se

*J.J. Jowais and S. Yazdi are co-first authors.

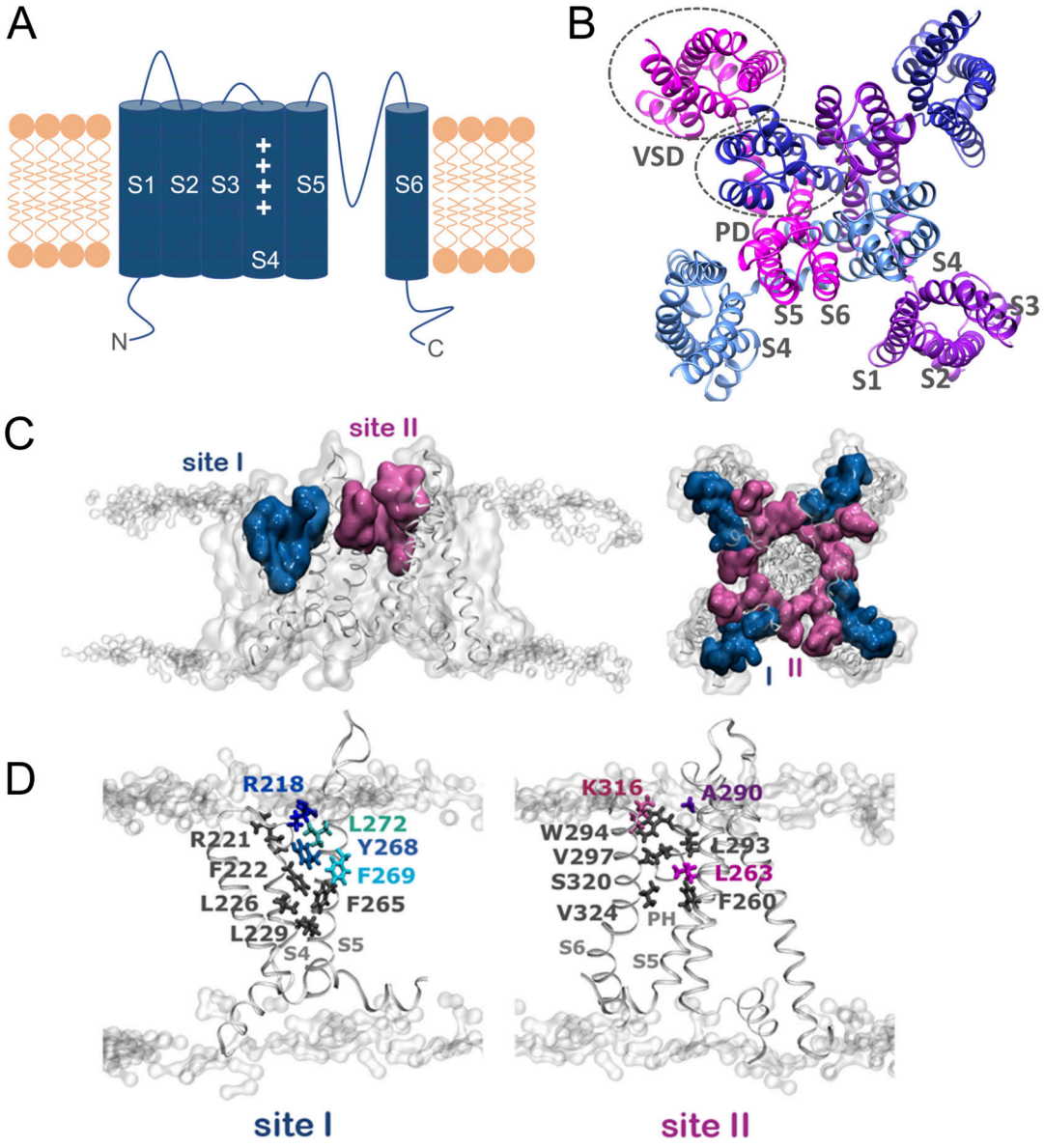

Figure 1. **Previously described binding Sites I and II for LIN. (A)** Sideview cartoon of KCNQ1 subunits S1–S6. **(B)** Top view of KCNQ1 with S1–S6 labeled and the voltage sensing domain (VSD) and pore domain (PD) circled. **(C)** Side and top view of binding site regions I and II for LIN. **(D)** Residues previously described in simulations to be important for LIN binding at Site I and II. Residues only suggested in simulation are shown in gray. Residues confirmed by mutation are shown in color. All simulation data and mutation data for L272, Y268, F269, A290, and L263 in this figure is from Yazdi et al. (2021). Mutation data for R218 and K316 is from Liin et al. (2018).

to more negative voltages and increase the maximum conductance (Fig. 2 B; Bohannon et al., 2020b; Liin et al., 2016; Liin et al., 2018). Since KCNQ1 is opened by positive changes in voltage, the voltage-dependence shift means the channels open with less depolarization, thus activating the channel. In addition, the increase in maximum conductance allows the channel to pass more potassium current once activated. These two effects are independent of each other and due to two separate binding sites on the KCNQ1 channel (Liin et al., 2018; Yazdi et al., 2021; Fig. 1 C). The shift in the voltage dependence is due to PUFA binding to Site I. Site I is located next to the S4 voltage sensor (Liin et al., 2018; Yazdi et al., 2021). The negative head group of the PUFA binds to positive charges of the voltage sensor. We believe this helps to stabilize the voltage sensor in the outward state, thereby shifting the voltage dependence to more negative voltages (Bohannon et al., 2020b; Liin et al., 2018). Specifically, our previous mutagenesis experiments show that residue R218 (R228 hKCNQ1) of the voltage sensor is necessary for this voltage dependence shift effect of PUFAs (Liin et al., 2018). Molecular dynamic (MD) simulations of linoleic acid (LIN) indicate R218 and F222 in S4, and Y268, F269, and L272 in S5 as high-contact residues at Site I (Yazdi et al., 2021; Fig. 1 D). The second effect PUFAs have on the KCNQ1 channel, increasing the maximum conductance, is due to PUFA binding at Site II. Site II is located near the pore domain (Liin et al., 2018; Yazdi et al., 2021; Fig. 1 C). Neutralizing mutations of K316 (K326 hKCNQ1) remove the

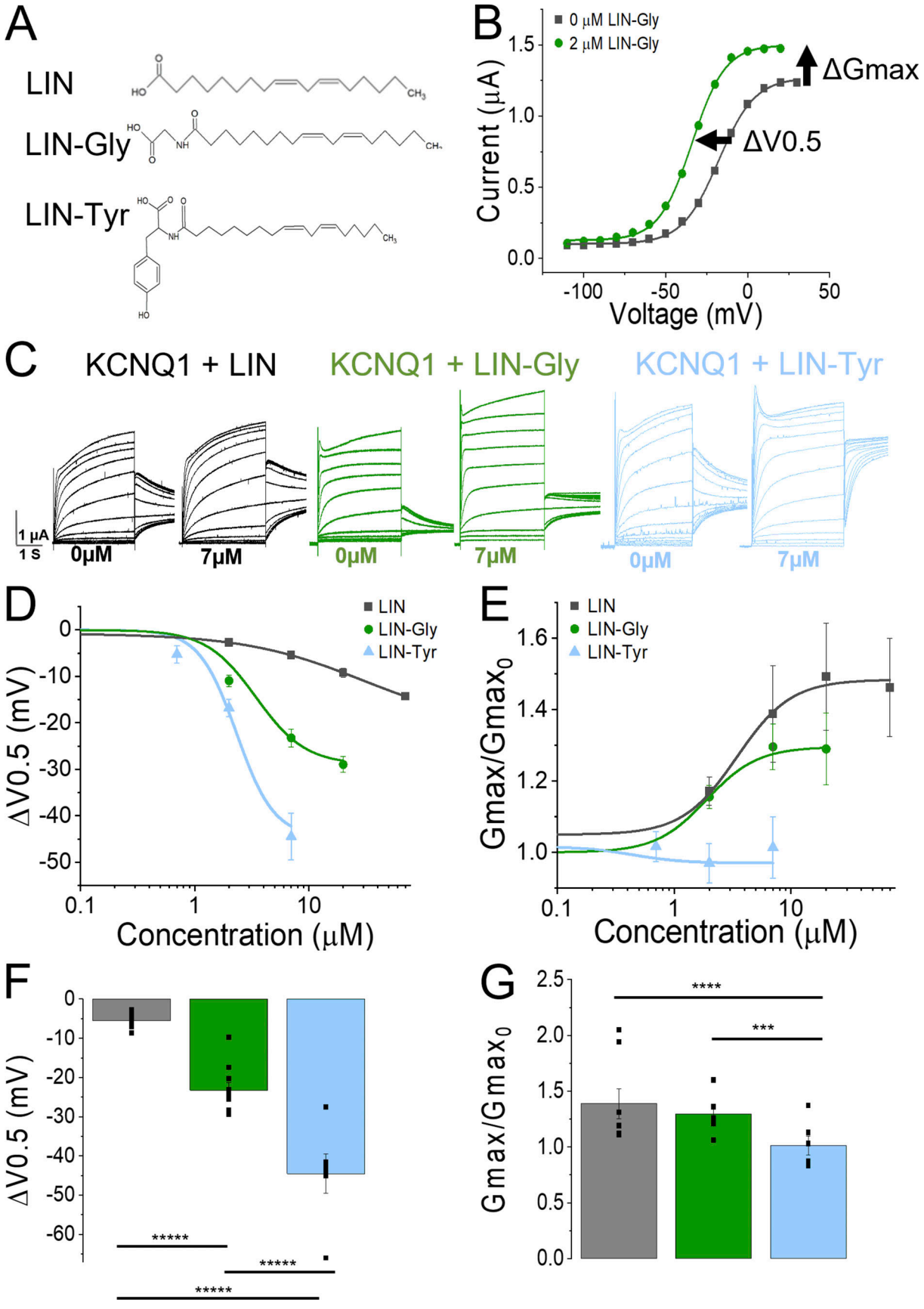

Figure 2. **LIN-Gly and LIN-Tyr have larger voltage shifts but smaller G_{max} increases as compared to LIN. (A)** Chemical structures of LIN, LIN-Gly, and LIN-Tyr. **(B)** Current of WT KCNQ1 with and without 2 μM of LIN-Gly, demonstrating the shift in voltage dependence toward negative voltages (ΔV0.5) and increase

in maximal conductance (ΔG_{max}) effects by addition of PUFA. **(C)** Current traces of KCNQ1 before and after application of 7 µM of LIN (black), LIN-Gly (green), and LIN-Tyr (blue). **(D)** ΔV0.5 dose-response curve of LIN (n = 8), LIN-Gly (n = 10), and LIN-Tyr (n = 6). **(E)** G_{max} dose-response curve of LIN (n = 8), LIN-Gly (n = 7), and LIN-Tyr (n = 6). **(F)** ΔV0.5 effect of LIN (−5.45 ± 0.69 mV; n = 8), LIN-Gly (−25.28 ± 1.69 mV; n = 10), and LIN-Tyr (−44.51 ± 5.05 mV; n = 6) at 7 µM. ANOVA with Tukey's multiple comparison gave P < 0.0001 between all compounds. **(G)** G_{max} effect of LIN (1.39 ± 0.13; n = 8), LIN-Gly (1.3 ± 0.06; n = 7) and LIN-Tyr (1.01 ± 0.09; n = 6) at 7 µM. ANOVA with Tukey's multiple comparison gave P < 0.0001 between LIN and LIN-Tyr, P = 0.0005 between LIN-Gly and LIN-Tyr, and P = 0.25 between LIN and LIN-Gly. Data are given as mean ± SEM. LIN data from Yazdi et al. (2021). ***, P < 0.001; ****, P < 0.0001.

PUFA effect on maximum conductance (Liin et al., 2018). The negative head group of the PUFA binds to K316 on S6 (Liin et al., 2018). In our previous MD simulations, residues I314 in S6 and F129 and Y138 in S1 are other high-contact residues for LIN binding at Site II (Yazdi et al., 2021; Fig. 1 D). The mechanism of how PUFA binding at Site II causes an increase in maximum conductance remains largely unknown.

Our previous electrophysiology experiments show that some PUFA analogs more strongly shift the voltage dependence of KCNQ1 as compared with regular PUFAs (such as LIN; Bohannon et al., 2020b). In this study, we combine MD simulations and electrophysiology experiments to detail how two PUFA analogs, linoleic–tyrosine (LIN-Tyr) and linoleic–glycine (LIN-Gly; Fig. 2 A), interact with the KCNQ1 channel. A comparison of how the interactions of these analogs with KCNQ1 differ from those of LIN may be used to further optimize the PUFA activation effect and aid the development of drugs based on the PUFA mechanism of activating KCNQ1 channels.

Materials and methods

Structure preparation

The 3-D structure used for the transmembrane domain of KCNQ1 channel (residues 94–348) was built using the structure of xKCNQ1 channel solved by cryo-EM at 3.7 Å (Sun and MacKinnon, 2017). The sequence similarity between the xKCNQ1 and hKCNQ1 channel is very high, 95% identical through S1–S6. Throughout the Results section, xKCNQ1 numbering of residues is used. For the mutational results on human IKs channels, the xKCNQ1 numbering is still used for ease of comparison; however, the human numbering is given in the figure legends. In this structure of KCNQ1, S4 is in an activated "up" position, whereas the pore is closed due to the absence of phosphatidylinositol 4,5-bisphosphate (PIP_2) in the cryo-EM structure (Sun and MacKinnon, 2017).

We started simulations with the same structure and preparations used previously for our LIN all-atom (AA) MD simulations of KCNQ1 in a lipid membrane (Yazdi et al., 2021). The channel was embedded into a lipid bilayer consisting of phosphatidylethanolamine:phosphatidylglycerol:cholesterol:FA (POPE:POPG:CHOL:FA) in a 3:1:1:1 ratio. KCNQ1 requires the presence of (PIP_2) lipids for its function; therefore, PIP_2 lipids were included in the inner leaflet in every bilayer simulation. The lipid composition for these systems was as follows: 307 POPE, 102 POPG, 88 CHOL, 16 PIP_2, and 117 FA. 63 FAs were distributed in the outer leaflet and 54 FAs in the inner leaflet. We changed the LIN molecules to either LIN-Gly or LIN-Tyr. Both PUFAs have an 18-carbon-long acyl tail with ω-6 unsaturation but differ in their head groups. LIN-Gly and LIN-Tyr have a glycine or tyrosine amino acid, respectively, attached at the LIN carboxyl group by an amide bond. These head groups are both larger than that of LIN (compare structures in Fig. 2 A). Both PUFA analogs in these simulations are in the deprotonated, negatively charged state. PUFA analogs are present in both leaflets in our simulations. We focus here on PUFA analogs in the extracellular leaflet because we have previously shown that PUFA binding from the inner leaflet had no functional effects (Yazdi et al., 2021).

AA MD simulations

AA production runs were performed for the following KCNQ1 systems: LIN-Gly Site I, LIN-Gly Site II, LIN-Tyr Site I, and LIN-Tyr Site II. The ANTON2 software version 1.27.0 from D.E. Shaw Research was used for production runs on the purpose-built ANTON2 supercomputer (Shaw, D.E., et al. 2014. Proceedings of the International Conference for High-Performance Computing, Networking, Storage and Analysis. https://doi.org/10.1109/SC.2014.9). The production runs were performed for 3 µs each using the CHARMM36M force field to assess structural dynamics of KCNQ1 in various membranes. The latest CHARMM36 lipid parameters were used to describe multicomponent membranes (Klauda et al., 2012). CHARMM-NBFIX LJ parameters for K^+ and Cl^- (Noskov and Roux, 2008) were used to simulate counter-ion dynamics with standard TIP3P water. The production runs were executed in a semi-isotropic (NPaT) ensemble at a temperature of 315°K maintained by the Nosé–Hoover thermostat (Martyna, 1994). Nonbonded and long-range electrostatic interactions were evaluated every 2 and 6 fs, respectively, using the RESPA multiple time-step algorithm (Tuckerman and Bechhoefer, 1992). Long-range electrostatics was calculated using the k-Gaussian Ewald method implemented to enhance performance on ANTON2 platform (Shaw, D.E., et al. 2014. Proceedings of the International Conference for High-Performance Computing, Networking, Storage and Analysis. https://doi.org/10.1109/SC.2014.9) with a 64 × 64 × 64 grid. SHAKE was used to constrain all bonds involving hydrogen atoms. The multi-integrator (multigrator) algorithm (Lippert et al., 2013) developed in-house by D.E. Shaw Research was used for temperature and semi-isotropic pressure coupling (Shaw, D.E., et al. 2014. Proceedings of the International Conference for High-Performance Computing, Networking, Storage and Analysis. https://doi.org/10.1109/SC.2014.9). The time step for production runs was set to 2 fs, and trajectories were saved every 500 ps. The structural integrity of the protein back bone was tested in our previous studies (Yazdi et al., 2021).

Analysis of FA enrichment regions and interaction sites in AA simulations

To identify the FA interaction sites in KCNQ1, we performed lipid–protein interaction analysis. An interaction is defined as

when an entire (i.e., both head group and tail) lipid molecule is located within 6 Å of the channel. PUFA interaction sites were identified by two separate measures: the total interaction time and the longest lifetime. The total interaction time calculates the total time of interaction observed between each residue and any FA (could be more than one FA at a time) over the last 2.5 µs of the simulation, regardless of the duration of each interaction. The longest lifetime, on the other hand, is a measure of the longest-lasting contact between each residue and any FA without any interruptions in the interaction. Using the maximum-likelihood method (Colquhoun et al., 1996), we also calculated the most likely average lifetime for the interactions for each residue. The total interaction time, average lifetime, and longest lifetime were averaged across the four channel subunits to account for the fourfold symmetry of the channel. Distances between FAs and the channel for the AA simulations were calculated with the MDTraj Python library. In-house R scripts were used to calculate the total interaction time made by each FA molecule over the course of the simulations. The FAs that stayed bound to the channel during the entire 2.5 µs simulation were identified by calculating the longest lifetime for each FA and are referred to as the "constant binders." Clustering was performed with the built-in Gromacs tool gmx cluster using the GROMOS method (Daura et al., 1999), with the distance cutoff set to 5 Å. By setting a distance cutoff, the GROMOS method takes the structure with the largest number of neighbors as the centroid of the first cluster and eliminates it from the pool of structures together with all its neighbors. This procedure is repeated for all remaining structures until all structures have been designated to a cluster. The center of each cluster, which is the structure with the smallest average root mean square deviation from all other structures of the cluster, was taken as the representative pose. Hydrogen bonds were considered to form when a hydrogen-bond donor, that is, a hydrogen atom bound covalently to an electronegative atom, was within a cutoff distance of 3.5 Å of an electronegative hydrogen-bond acceptor. As a definition of salt bridge formation, we considered a cutoff of 4 Å between N-O atom pairs.

Molecular biology

KCNQ1 (UniProt: P51787) complementary RNA was transcribed using the mMessage mMachine T7 kit (Ambion). 50 ng of complementary RNA was injected into defolliculated *Xenopus* oocytes (Ecocyte) for KCNQ1 channel expression. Site-directed mutagenesis was performed using the Quickchange II XL Mutagenesis Kit (Qiagen Sciences) for mutations in KCNQ1. Injected cells were incubated for 72–96 h in standard ND96 solution (96 mM NaCl, 2 mM KCl, 1 mM MgCl2, 1.8 mM CaCl2, and 5 mM HEPES; pH 7.5) containing 1 mM pyruvate at 16°C before electrophysiological recordings.

Two-electrode voltage clamp

Xenopus oocytes were recorded in the two-electrode voltage-clamp configuration. Recording pipettes were filled with 3 M KCl. The chamber was filled with ND96 recording solution (mM NaCl, 2 mM KCl, 1 mM $MgCl_2$, 1.8 mM $CaCl_2$, and 5 mM HEPES; pH 7.5). PUFAs were obtained from Cayman Chemical or were synthesized in-house (University of Linköping) and kept at −20°C as 100 mM stock solutions in ethanol. PUFAs were perfused into the recording chamber using the Rainin Dynamax Peristaltic Pump (Model RP-1). Electrophysiological recordings were obtained using Clampex 10.3 software (Axon, pClamp; Molecular Devices). To record KCNQ1 currents, the holding voltage was generally set to −80 mV. Activation curves were generally generated in steps between −80 and +60 mV in increments of 10 mV (3-s duration). The tail voltage was set to −30 mV. PUFAs were perfused in preapplication step until effect on current amplitude reached steady state or for a minimum of 5 min. The chamber was cleaned between each oocyte using a 70% ethanol solution.

Electrophysiological analysis

To quantify the voltage dependence for channel opening, tail currents were measured shortly after stepping to the tail voltage and plotted against the preceding activation voltage. A Boltzmann function was fitted to the data to generate the conductance versus voltage (G(V)) curve:

$$G(V) = G_{\min} + (G_{max} - G_{min}) / \{1 + \exp[(V_{0.5} - V)/s]\}, \quad (1)$$

where G_{min} is the minimal conductance, G_{max} is the maximal conductance, V0.5 is the midpoint (i.e., the voltage at which the conductance is half the maximal conductance determined from the fit), and s is the slope of the curve. The difference in V0.5 induced by LIN-Gly or LIN-Tyr in each oocyte (i.e., ΔV0.5) was calculated to quantify the shift in the voltage dependence for channel opening. The difference in G_{max} induced by LIN-Gly or LIN-Tyr in each oocyte (i.e., ΔG_{max}) was calculated to quantify the change in the maximal conductance.

To plot the concentration dependence of the LIN-Gly or LIN-Tyr induced effect on V0.5 or G_{max} as a function of the PUFA concentration, the following concentration-response curve was fitted to the data:

$$\Delta V_{0.5} = A / \left[1 + ([PUFA]_{50}/[PUFA])^H\right] \quad (2)$$

$$G_{max} / G_{max}0 = 1 + B / \left[1 + ([PUFA]_{50}/[PUFA])^H\right], \quad (3)$$

where A is the maximal shift in V0.5, B is the maximum relative increase in $G_{max}\{B = (G_{max} - G_{max}0)/G_{max}0\}$, $[PUFA]_{50}$ is the PUFA concentration needed to cause 50% of the maximal effect, and H is the Hill coefficient. The limited solubility of LIN-Tyr at concentrations of about 20 µM prevented us from quantifying this PUFA's effect at higher concentrations. Therefore, the Hill coefficient of the concentration-response curves was constrained 1 to make the fits more robust. Average values are expressed as mean ± SEM. Statistics were calculated using either one-way ANOVA followed by Dunnett's multiple comparisons test (to compare with WT) or one-sample *t* test (to compare with a hypothetical value). $P < 0.05$ was considered statistically significant.

Online supplemental material

Fig. S1 shows the most likely length of lifetime interactions for LIN-Tyr at each residue from maximum likelihood fits of data in Fig. 3. Fig. S1 also shows the total number of LIN-Tyr binding

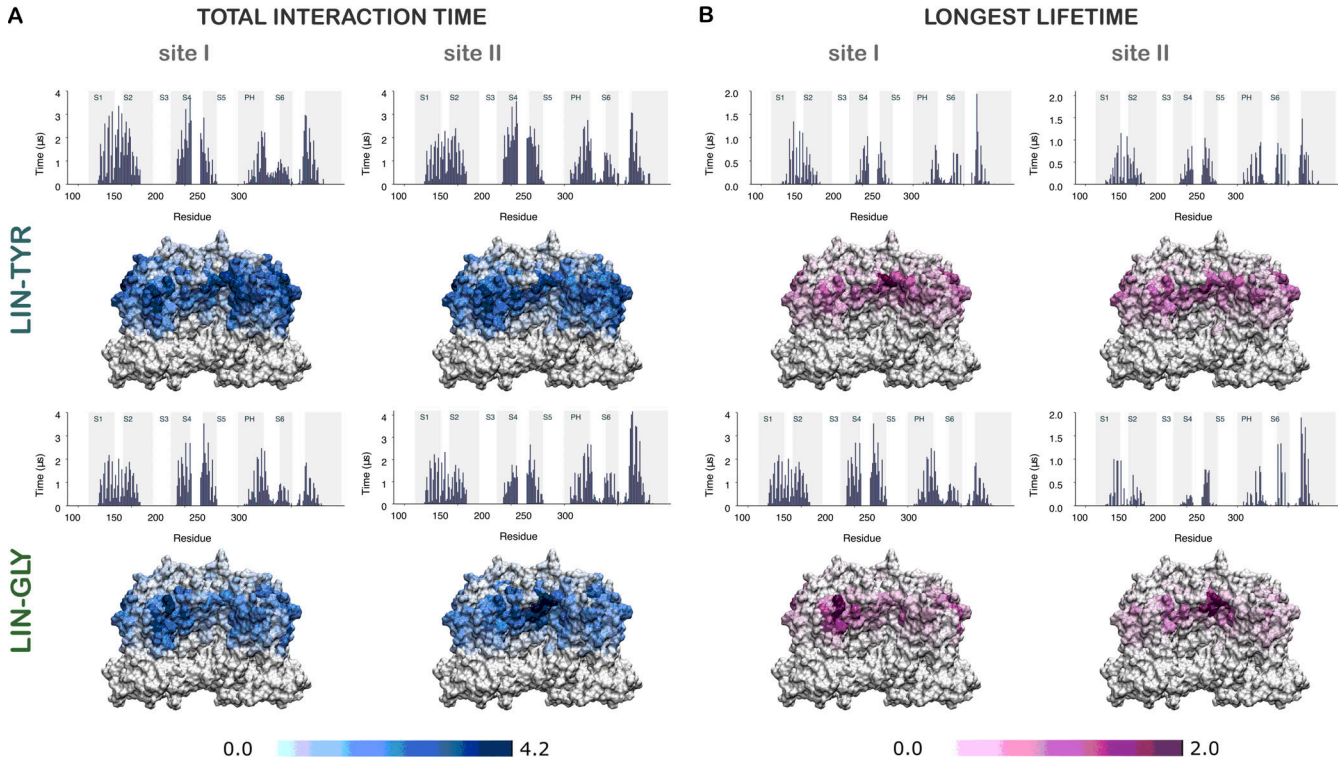

Figure 3. **LIN-Gly and LIN-Tyr interact with many residues on the KCNQ1 channel.** Contact analysis for AA LIN-Gly and LIN-Tyr simulations. The gray highlighted boxes in the background indicate the position of the transmembrane helices. **(A)** Histogram and heat map of total interaction time of each residue in KCNQ1 for LIN-Tyr and LIN-Gly in the Site I and Site II systems. **(B)** Histogram and heat map of longest lifetime interactions of each residue in KCNQ1 for LIN-Tyr and LIN-Gly in the Site I and Site II systems.

events with each residue. Fig. S2 shows the most likely length of lifetime interactions for LIN-Gly at each residue from maximum likelihood fits of data in Fig. 3. Fig. S2 also shows the total number of LIN-Gly binding events with each residue.

Results

LIN-Tyr and LIN-Gly have increased effects on voltage-dependence shift and decreased effects on maximum conductance as compared with LIN in KCNQ1

We have previously shown that different PUFA analogs can have superior effects on KCNQ1 activation compared with regular PUFAs, such as LIN. Here, we compare the effects of PUFA analogs LIN-Gly and LIN-Tyr to the effects of LIN using two-electrode voltage clamp experiments on KCNQ1 channels expressed in *Xenopus* oocytes. The application of PUFA in general shifts the voltage dependence to the left and increases the maximum conductance of KCNQ1 channels (Liin et al., 2018). We measure these PUFA effects to get the $\Delta V0.5$ and ΔG_{max} (Fig. 2 B). LIN-Gly and LIN-Tyr shift the voltage dependence of KCNQ1 to more negative voltages than LIN (Fig. 2, D and F). LIN-Tyr has a bigger effect then LIN-Gly on this voltage dependence shift (Fig. 2, D and F). However, LIN-Tyr had less effect on the increase in maximum conductance than LIN (Fig. 2, E and G). LIN-Gly caused an increase in maximum conductance that was in between LIN and LIN-Tyr (Fig. 2, E and G). Our previous results from studies with LIN suggest that the shifts in voltage dependence are due to PUFAs binding at Site I and the increases in maximum conductance are due to PUFAs binding at Site II (Fig. 1, C and D). The residues found to be important from simulation and mutational studies for LIN binding at these sites are indicated in Fig. 1 D. However, the mechanisms by which the PUFA analogs, LIN-Gly and LIN-Tyr, shift the voltage dependence more effectively and increase the maximum conductance less effectively are currently unknown.

LIN-Tyr and LIN-Gly bind to similar sites as LIN on KCNQ1

To understand why LIN-Gly and LIN-Tyr have bigger voltage shift effects (most likely through Site I) and less G_{max} effects (most likely through Site II) of the KCNQ1 channel, we conducted microseconds long AA MD simulations in a multicomponent membrane bilayer with a lipid composition of POPE, POPG, CHOL and PIP_2 (inner leaflet only), and PUFA analogs (LIN-Gly and LIN-Tyr) added to both leaflets. These simulation systems were identical to our previous simulations of LIN interactions with KCNQ1 (Yazdi et al., 2021), in which the levels of the different lipids were chosen to be comparable to the concentrations in simplified models of the cardiomyocyte membrane (Marrink et al., 2019). To determine how LIN-Gly and LIN-Tyr interact with KCNQ1, four simulations systems were created based on our previous simulations with a LIN molecule bound either at Site I or II in KCNQ1 (Yazdi et al., 2021). In these fours systems, we now replaced all LIN molecules with either LIN-Gly or LIN-Tyr, thereby creating "LIN-Gly site I," "LIN-Gly site II," "LIN-Tyr site I," and "LIN-Tyr site II" starting systems.

During the 3-μs simulation of the four starting systems, several LIN analogs bound and unbound from the different sites on KCNQ1, similar to how LIN interacted with KCNQ1 (Fig. 3; Yazdi et al., 2021). We plotted the total interaction time, the total time of interaction between each residue and an FA, and longest lifetime, the longest lasting contact between each residue and an FA (Fig. 3). Using the Maximum-Likelihood method (Colquhoun et al., 1996), we also calculated the most likely average lifetime for the interactions for each residue (Figs. S1 and S2). There were two well-separated clusters of lifetimes for most residues: one with a lifetime of around 5 ns (Figs. S1 and S2), which we attribute to random interaction events with a lifetime governed by PUFA diffusion in the lipid bilayer, and one longer one (100s–1,000s ns; Figs. S1 and S2) that we attribute to the actual binding events of PUFAs to the channel. The frequency of interactions between the PUFA analogs and KCNQ1 were high enough that the actual starting system (i.e., starting with a PUFA analog in Site I or Site II) had very minor effect on the graphs (Fig. 3), suggesting that 3 μs is long enough to capture most interactions between PUFA analogs and KCNQ1. To resolve long-lasting interactions between LIN analogs and KCNQ1, we focused our detailed analysis on the "constant binders," which were the molecules that stayed bound during the entire simulation.

Three of the LIN-Gly constant binders interacted with S4, with the Gly head group stabilized at S4 through interactions with the positively charged residues R218 and R221, which are the two outermost gating arginines in KCNQ1 (i.e., R1 and R2; Fig. 4 A). The LIN tail showed more mobility than the head group by exploring a relatively extensive hydrophobic lipid-exposed surface of S3, S4, and S5, including residues P222 and L226 on S4. Additional polar or hydrophobic residues interacting with the LIN-Gly head and tail engaged two networks of residues depending on whether LIN-Gly was on the S5 or S3 side of S4, which will be referred to as Site Iα and Site Iβ, respectively (Yazdi et al., 2021). Residues S215, V202, and V205 engaged in interactions at the S3 side and residues K275, Y268, and Y271 on the S5 side (Fig. 4 A). Two of the LIN-Gly constant binders interacted with S6, with the Gly head group stabilized at S6 through interactions with the positively charged residue K316 and negatively charged D291, forming a hydrogen bond with the NH in the glycine head group, and the LIN tail interacting with hydrophobic residues on S6, S5, and S1 (e.g., P260, L263, and W294; Fig. 4 A).

LIN-Tyr interacted with overall similar residues on KCNQ1 to those of LIN-Gly, with Tyr head group interactions with R218, R221 (at S4), and K316 (at S6) and many interactions with primarily hydrophobic residues in each site (Fig. 4 C). However, LIN-Tyr only bound to Site Iβ and not Site Iα in these simulations. Moreover, compared with LIN-Gly, the LIN-Tyr head group was more mobile by exploring a larger set of conformations (compare the red representation of head group poses of LIN-Gly and LIN-Tyr; Fig. 4 C). One LIN-Tyr molecule was bound at a site in-between S5 and S6 not observed for LIN-Gly. However, this tentative S5–S6 site of LIN-Tyr likely represents a transition site when LIN-Tyr molecules explore the KCNQ1 surface, as no consistent mode of LIN-Tyr interaction was observed for this site. Altogether these interactions show both LIN-Gly and LIN-Tyr bind to similar sites previously described for LIN, with the exception of LIN-Tyr at Site Iα (Yazdi et al., 2021).

LIN-Gly and LIN-Tyr shift KCNQ1 voltage dependence through S4 charges

Experimentally, we have seen that LIN-Gly and LIN-Tyr shift the voltage dependence more than LIN (Fig. 2, D and F). LIN shifts the KCNQ1 voltage dependence via interactions between its negative head group and the positive charges in the voltage sensor, one very important residue in the hKCNQ1 channel being R218 (R228 hKCNQ1). It has been suggested that this interaction stabilizes the voltage sensor in the upward state, thus shifting the voltage dependence to more negative voltages (Fig. 5 A). To determine if LIN-Gly and LIN-Tyr are acting via a similar mechanism to shift the voltage dependence, we performed voltage-clamp experiments on the human KCNQ1 channel with the mutation R218Q (R228Q hKCNQ1) and compared the shifts in voltage dependence of LIN, LIN-Gly, and LIN-Tyr (Fig. 5). The R218Q mutation itself shifts the voltage dependence of the KCNQ1 channel, but the currents are not further shifted by the addition of the PUFAs (Fig. 5 B). These experiments show that residue R218 is vital for the shifts in the voltage dependence of all three PUFAs (Fig. 5). This suggests that the PUFA analogs LIN-Gly and LIN-Tyr are also shifting the voltage dependence by stabilizing the voltage sensor in the upward state.

LIN-Tyr interacts more with Site Iβ than LIN-Gly and less specifically at Site II

The analysis of total interaction time and longest lifetime included all LIN analogs in the systems and showed that both LIN-Gly and LIN-Tyr interact with a large set of residues in KCNQ1, with the longest total interaction time and lifetime were observed for residues in the upper half of each of the transmembrane helices, or in the extracellular loops connecting these (Fig. 3). The most long-lived interactions were observed with residues in or near the top of S4 (e.g., R218, G219, P220, V202, and V205) and in or near the top of S6 (e.g., W313, T317, I314, L293, A290, and K316). In addition, in particular, LIN-Tyr showed long-lived interactions with residues in the top of S1 and S2 (e.g., L132, Y138, and L141). Plotting all residues in the upper half of the channel with a total interaction time longer than 2 μs highlights the preferred regions of LIN-Gly and LIN-Tyr interaction (Fig. 6), which show that both LIN analogs interact with residues in the extracellular half of all transmembrane helices S1–S6. However, LIN-Tyr interacts with more Site Iβ residues, between S3 and S4, than LIN-Gly (Fig. 6), and this further suggests that LIN-Tyr prefers Site Iβ. LIN-Tyr also interacts more diffusely in Site II versus LIN-Gly (Fig. 6), this could help to explain why LIN-Tyr has less of a G_{max} effect than LIN-Gly.

LIN-Gly and LIN-Tyr head groups enable several simultaneous interactions with KCNQ1

Although LIN-Gly and LIN-Tyr overall interact with similar sites to those previously identified for LIN, there were important

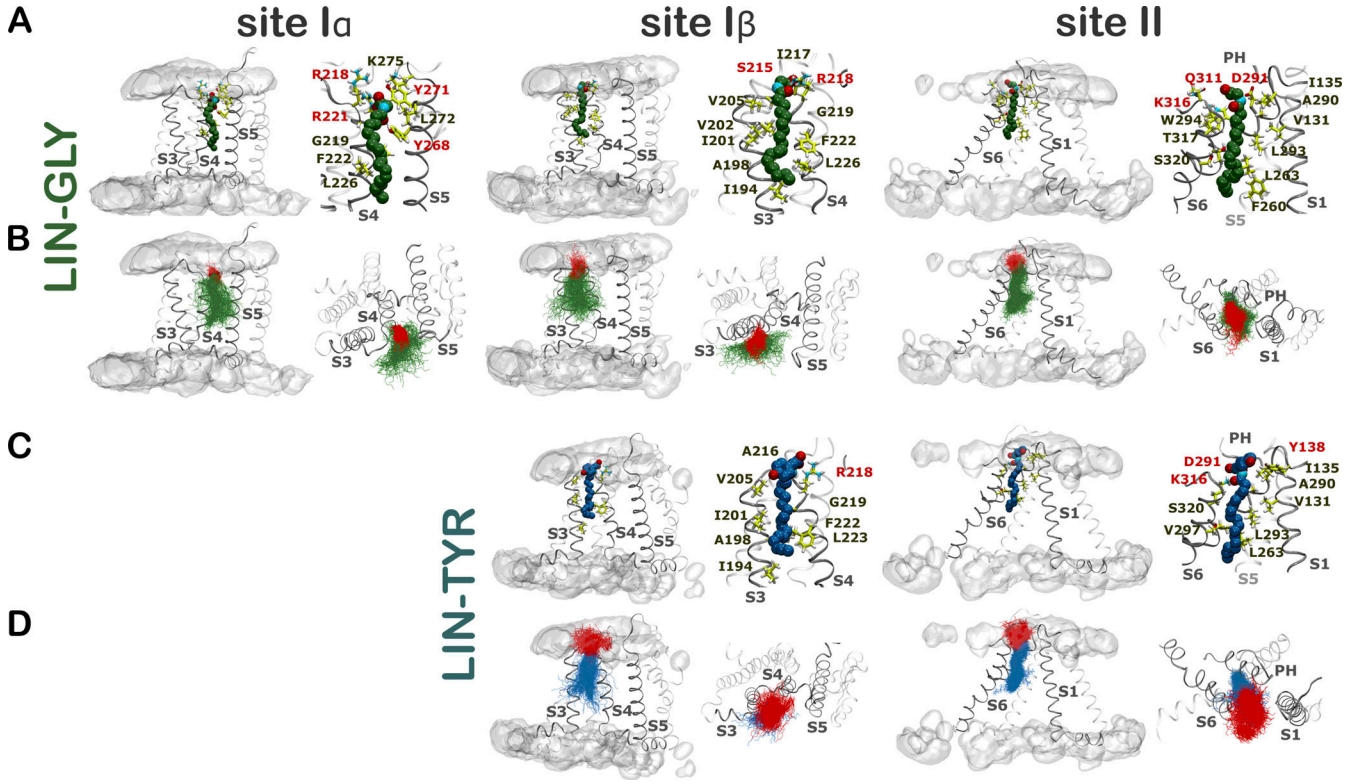

Figure 4. **Representative poses of a LIN-Gly and LIN-Tyr constant binders at previously described Sites Iα and Iβ and Site II.** Site I was split into Site Iα and β to better show the two major but different confirmations of PUFAs at Site I. We have previously published this separation of Site I into Site Iα and β in Yazdi et al. (2021). Red residues are making head group interactions with the PUFAs. **(A)** Side view of representative LIN-Gly constant binder at Sites Iα, Iβ, and II. **(B)** Overlay of all LIN-Gly constant binder poses at Sites Iα, Iβ, and II. The LIN-Gly head group is shown in red and the tail in green. **(C)** Side view of representative LIN-Tyr constant binder at Sites Iβ and II. **(D)** Overlay of all LIN-Tyr constant binder poses at Sites Iβ and II. The LIN-Tyr head group is shown in red and the tail in blue.

differences in the modes of interaction attributed to the different head group chemistry. Total percent interaction time of LIN-Gly and LIN-Tyr constant binder head groups at each binding site shows that they make multiple high percentage interactions throughout the simulation at Site I (Fig. 7, A and B). This indicates that there are simultaneous interactions of residues taking place. In many cases, the sum of total percent of interaction time at a site for either PUFA is greater than 100%, and for these cases, the probability that these head groups are interacting with multiple residues at a time is even stronger. These simultaneous interactions are not seen in our previous simulations of LIN (Yazdi et al., 2021).

At Site Iβ (S3–S4), the LIN-Gly constant binder head group interacts with S215 74% and R218 57% of the time in simulation (Fig. 7 A). This indicates that for at least 31% and a maximum of 57% of the time in the simulation, these residues were interacting with the LIN-Gly head group simultaneously. For the amount of time that at least one of these two residues interacted with the constant binder head group, there could be simultaneous interaction of both residues with the head group of up to 77% of the time. LIN-Tyr interacts with R218 82% and S215 2% of the time, indicating only a small possibility for head group simultaneous interactions in this case (Fig. 7 A). At Site Iα simultaneous interactions are even more prevalent for LIN-Gly. The LIN-Gly head group interacts with R218 10%, Y271 9%, R221 100%, and Y268 100% of the time in simulation (Fig. 7 B). At this site, it appears that R221 and Y268 are always simultaneously interacting with LIN-Gly while R218 and Y271 can also contribute for small amounts of time. In previous studies, LIN was shown to also interact with R221, R218, and R221 at Site I, but is not able to interact with them simultaneously (Yazdi et al., 2021). LIN-Tyr does not bind to Site Iα in our simulations.

At Site II, LIN binds to the residue K316 98% of the time in simulation (Yazdi et al., 2021). LIN-Gly and LIN-Tyr interact with K316 only 41% and 36% of the time in simulation, respectively (Fig. 7 C). This indicates that these larger head groups may not fit well into the confined Site II and are less able to bind to the residue K316. K316 is very important for PUFA G_{max} effect (Liin et al., 2018), so this could explain why LIN-Gly and LIN-Tyr have less effect on G_{max} than LIN.

Electrophysiology experiments support the importance of predicted head group interactions

To experimentally test how the residues determined from our simulations affect LIN-Gly and LIN-Tyr binding, we performed two-electrode voltage-clamp recordings of KCNQ1 channels with those residues mutated and applied these two PUFA analogs. Simulations predict that while LIN-Gly binds to both Site Iα and Iβ, LIN-Tyr only binds to Site Iβ. Residues Y268 and K275 were predicted to participate in LIN-Gly binding at Site Iα. To test the

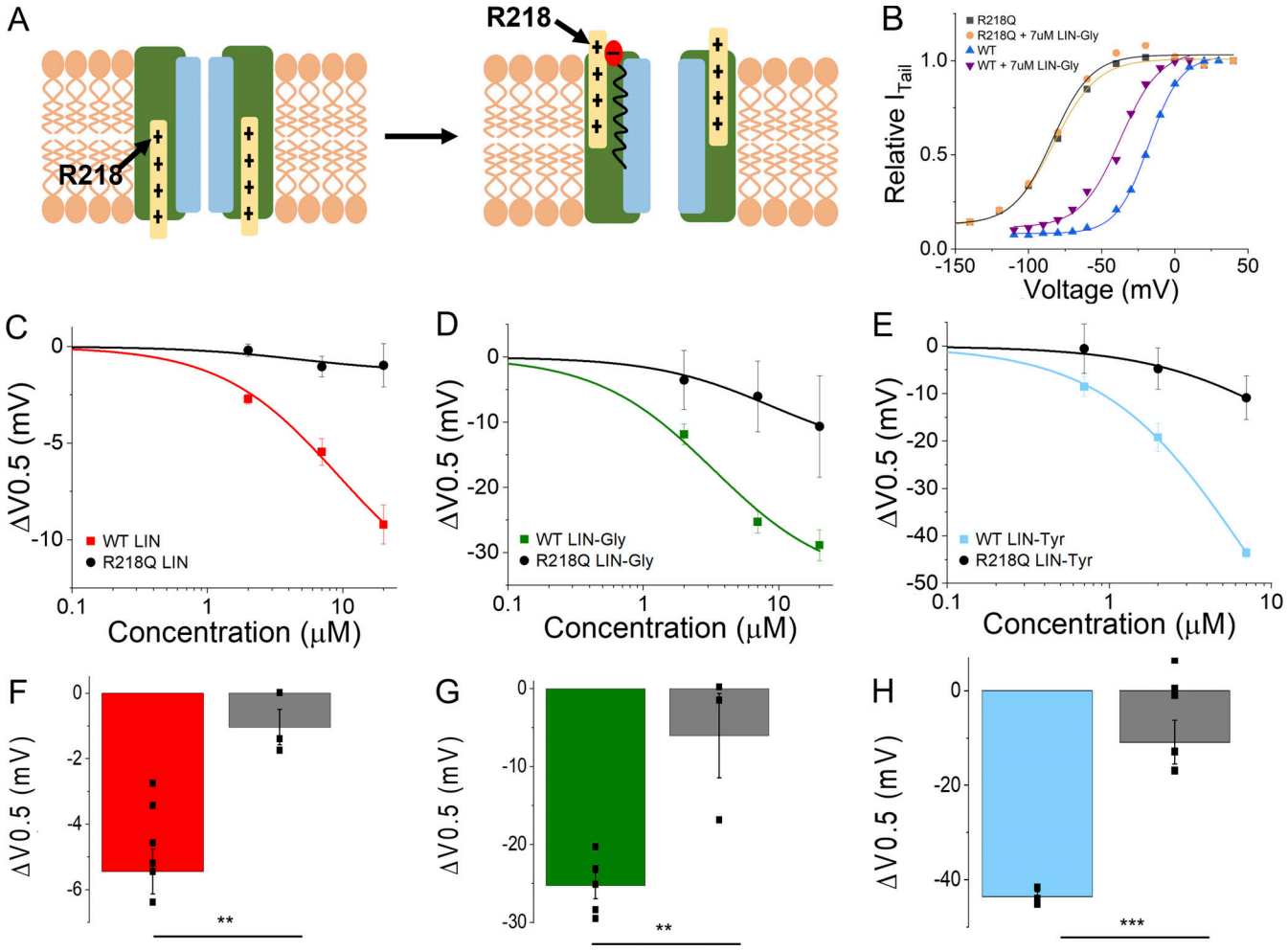

Figure 5. **LIN, LIN-Gly, and LIN-Tyr require residue R218 to maintain their voltage dependence shifting effect.** Experiments were done on the human KCNQ1 channel with the mutation R228Q; the *Xenopus* numbering R218 is used here for ease of comparison with the simulations. **(A)** Model of PUFA interaction with S4 that causes the V0.5 shifting effect, with residue R218 in the voltage sensor marked. **(B)** Conductance versus voltage (G(V)) curve of the R218Q and WT KCNQ1 currents with and without 7 μM of LIN-Gly. **(C–E)** ΔV0.5 dose response curve of (C) LIN (WT n = 8 and R218Q n = 3), (D) LIN-Gly (WT n = 10 and R218Q n = 3), and (E) LIN-Tyr (WT n = 6 and R218Q n = 5) on WT versus R218Q mutated KCNQ1 channels. Data are shown as mean ± SEM. **(F–H)** Comparison of ΔV0.5 effect on WT KCNQ1 channels versus R218Q mutated channels at 7 μM of (F) LIN (WT: −5.45 ± 0.69 mV; n = 8 and R218Q: −1.04 ± 0.54 mV; n = 3); a t test gave P = 0.005; (G) LIN-Gly (WT: −25.28 ± 1.69 mV; n = 10 and R218Q: −6.03 ± 5.43 mV; n = 3); ANOVA with Tukey's multiple comparison, also containing the mutations in Fig. 8, gave P = 0.0015; (H) LIN-Tyr (WT: −43.57 ± 1.03 mV; n = 6 and R218Q: −10.89 ± 4.61 mV; n = 5), ANOVA with Tukey's multiple comparison, also containing the mutations in Fig. 8, gave P = 0.0018. Data are shown as mean ± SEM. **, P < 0.01; ***, P < 0.001.

prediction from the simulations that LIN-Tyr does not bind to Site Iα and LIN-Gly does, we applied each PUFA on mutations of these two residues in Site Iα. LIN-Gly had significantly decreased effects on the voltage dependence shift of mutant Y268F (hKCNQ1 Y278F) and K275C (hKCNQ1 K285C) compared with WT KCNQ1 (Fig. 8, A and C). In contrast, the voltage shift effect of LIN-Tyr was not affected by either of these mutations (Fig. 8, B and D). This indicates that LIN-Tyr does not bind to Site Iα while LIN-Gly does. The mutation Y271F (hKCNQ1 Y281F) had no effect on either LIN-Gly or LIN-Tyr (Fig. 8). This is in line with the simulations, as residue Y271 only interacted with the PUFAs for small amounts of time throughout the simulation: 13% for LIN-Tyr and 9% for LIN-Gly (Fig. 7). These results show residue Y268 and K275 as important residues for the voltage dependence shifting effect of LIN-Gly on KCNQ1 and suggest that LIN-Tyr only binds to Site Iβ.

Discussion

We found that the PUFA analogs LIN-Tyr and LIN-Gly have larger effects on the voltage dependence of KCNQ1 channels compared with the regular PUFA LIN, while having decreased effects on G_{max} (Fig. 2). In our AA MD simulations, LIN-Tyr and LIN-Gly bind to similar sites as LIN on KCNQ1: Site I close to the voltage sensor S4 to affect the voltage dependence of the channel and Site II close to the pore domain of KCNQ1 to affect the G_{max} (Figs. 3 and 4). Our simulations suggest that the decreased effect of LIN-Gly and LIN-Tyr on G_{max} is due to that these two PUFA analogs do not spend as much time at the effector site in Site II (K316) as LIN, but, instead, these PUFA analogs interact with a range of residues nearby to Site II. However, the molecular mechanisms of why LIN-Gly and LIN-Tyr have an increased effect on voltage dependence are different between these two PUFA analogs. LIN-Gly is able to bind to more residues

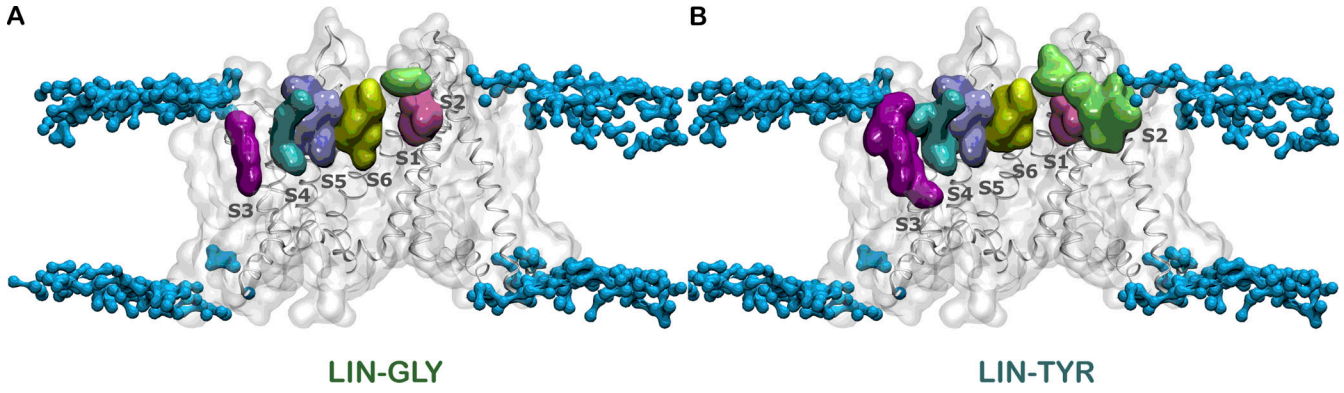

Figure 6. **LIN-Gly has a more condensed pattern of interaction than LIN-Tyr.** Regions of LIN-Gly and LIN-Tyr binding on the KCNQ1 channel. **(A)** Map of residues with interaction times longer than 2 µs with LIN-Gly molecules. **(B)** Map of residues with interaction times longer than 2 µs with LIN-Tyr molecules.

simultaneously at Site I, and we propose that this anchors LIN-Gly better in the binding site to increase the affinity and also places the negative headgroup of LIN-Gly in a better location to interact with the positive charges in S4 to increase the efficacy. Our mutational study and simulations suggest that LIN-Tyr binds to a variant of Site I (Site Iβ), and we propose that binding to Site Iβ is more effective in shifting the voltage dependence of the channel.

According to the proposed mechanism by which PUFAs shift the voltage dependence, known as the lipoelectric hypothesis, the lipid tail is embedded within the membrane and interacts with specific residues in the transmembrane segments of the channel close to the voltage sensor S4. This allows the negative PUFA head group to interact with the positive charges on the voltage sensor. The electrostatic interaction of the PUFA head group with the voltage sensor stabilizes it in the upward position, and thus the channel in the open state, while the lipid tail interacts with other residues to hold the PUFA in place next to the voltage sensor. We have shown with multiple different PUFAs that if you eliminate one of these voltage sensor charges, you remove or significantly diminish the shifts in voltage dependence by the PUFAs (Liin et al., 2015; Bohannon et al., 2020b). Since LIN-Gly and LIN-Tyr have a significant increase in ability to shift the voltage dependence, as compared to previous PUFAs, we, therefore, investigate here whether LIN-Gly and LIN-Tyr act on the voltage sensor charges. We show in this paper that a mutation of one of the positive charges in the voltage sensor (R218Q) decreases the shifts in voltage dependence induced by LIN-Gly and LIN-Tyr (Fig. 5). This indicates that LIN-Gly and LIN-Tyr shift the voltage dependence of KCNQ1 by stabilizing the voltage sensor in the upward state by interacting with the positive charges in S4.

To better understand why LIN-Gly and LIN-Tyr shift the voltage dependence more compared to LIN, we analyzed specifically the interaction times of the head groups of the constant binders (Fig. 7). We found that both LIN-Gly and LIN-Tyr form more simultaneous interactions than LIN (Fig. 7 B). Most notably, in Site Iα, LIN-Gly interacts for very large percentages of time with both residues R221 and Y268. We previously found that LIN also interacts with these residues; however, LIN is unable to do so simultaneously, due to the smaller head group of LIN (Yazdi et al., 2021). In our previous LIN simulations, we found that Y268 acts as an anchor point for LIN to bind to Site I while the voltage sensor is down, keeping the PUFA in place until it is able to switch from Y268 and bind to R218 when S4 has moved up (Yazdi et al., 2021). In this study, we see that the larger glycine head group is able to span the distance between R218 and Y268 to interact with R218 and Y268 at the same time (Fig. 7). The LIN-Gly head group was also shown from simulation and mutational experiments to interact with K275 at Site Iα. These additional interactions could increase LIN-Gly binding to Site Iα, explaining the increased affinity we see for LIN-Gly over LIN. These interactions could also position the negative charge on the carboxyl group of LIN-Gly closer to the positive charges in the voltage sensor, explaining the increase in the effect of LIN-Gly over LIN. All three compounds bind to Site Iβ in our simulations. However, LIN-Tyr is the only one to bind exclusively to Site Iβ and not to Site Iα. LIN-Tyr only binding to Site Iβ could explain the increased effectiveness of LIN-Tyr on shifting the voltage dependence versus that of LIN-Gly, if Site Iβ is more functionally effective. We propose that Site Iβ allows for the negative charge on the carboxyl group of LIN-Tyr to be better positioned to attract the voltage sensor upward than in Site Iα. At both Site Iα and Site Iβ, for all the compounds, the lipid tails have many interactions with hydrophobic residues on the channel, helping to anchor the PUFAs in the binding site. The residues L272 and F269 have previously been shown in mutational studies for LIN to participate in the binding to the channel (Yazdi et al., 2021). In general, all of these additional interactions with residues in binding Site I α and β (such as Y268, K275, L272, and F269) help to increase binding affinity or better anchor the PUFA so that the carboxyl group of the PUFA analogs can interact more strongly with the positive charges in the voltage sensor to cause an increased shift in voltage dependence.

The ability of PUFAs to increase the G_{max} of KCNQ1 has been linked to interactions with residue K316 (Yazdi et al., 2021). In this study, the highest interaction times at Site II head group was 41% at K316 for LIN-Gly and 36% at K316 for LIN-Tyr (Fig. 7 C). In contrast, LIN interacts with K316 in 98% of the conformations (Yazdi et al., 2021). Site II has a much more confined binding

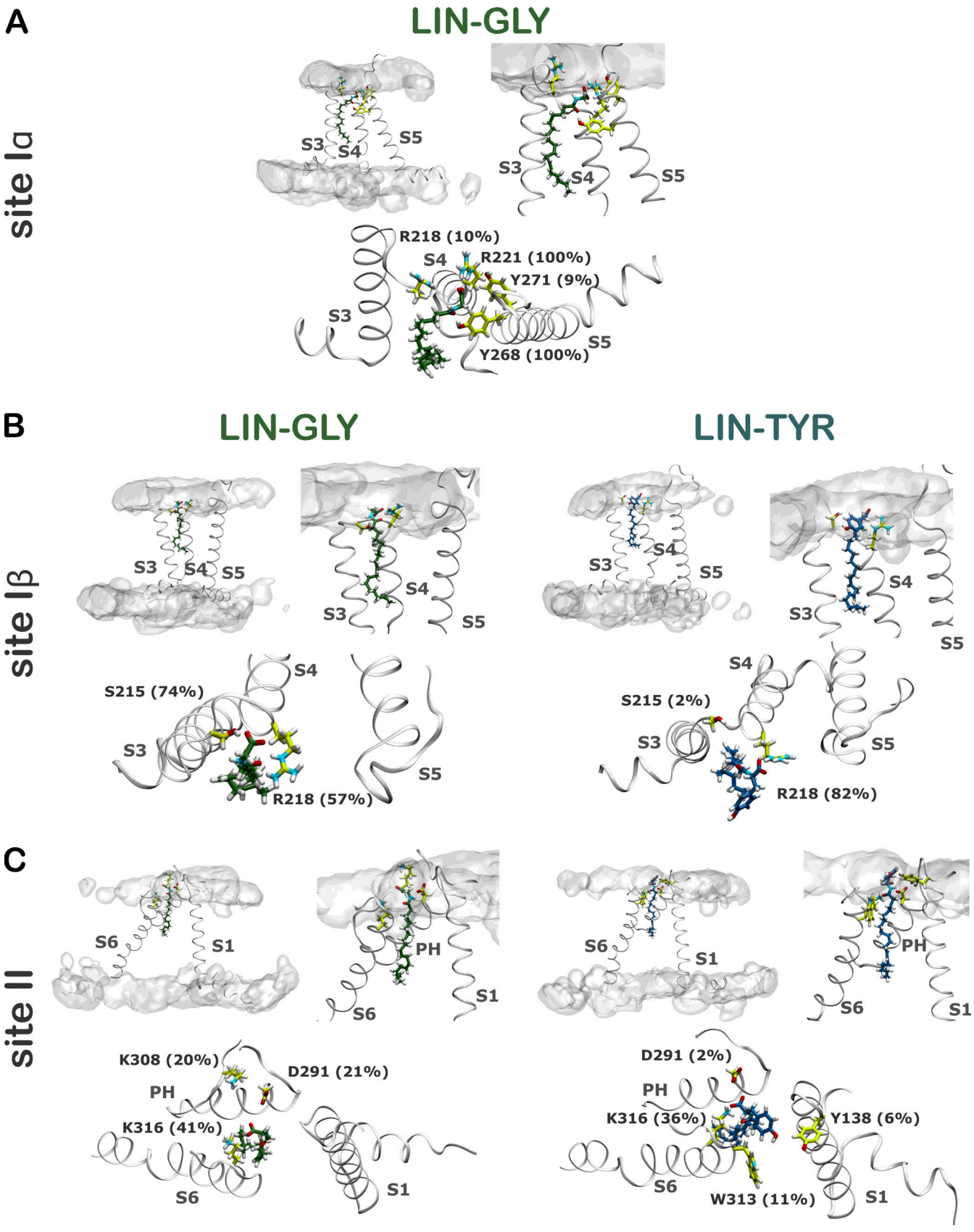

Figure 7. **Larger head groups allow for more and simultaneous interactions.** Each residue is shown with the percent of time it is interacting with the PUFA throughout the simulation. **(A)** Representation of constant binders of LIN-Gly in Site Iα. **(B)** Representation of constant binders of LIN-Gly and LIN-Tyr in Site Iβ. **(C)** Representation of constant binders of LIN-Gly and LIN-Tyr in Site II.

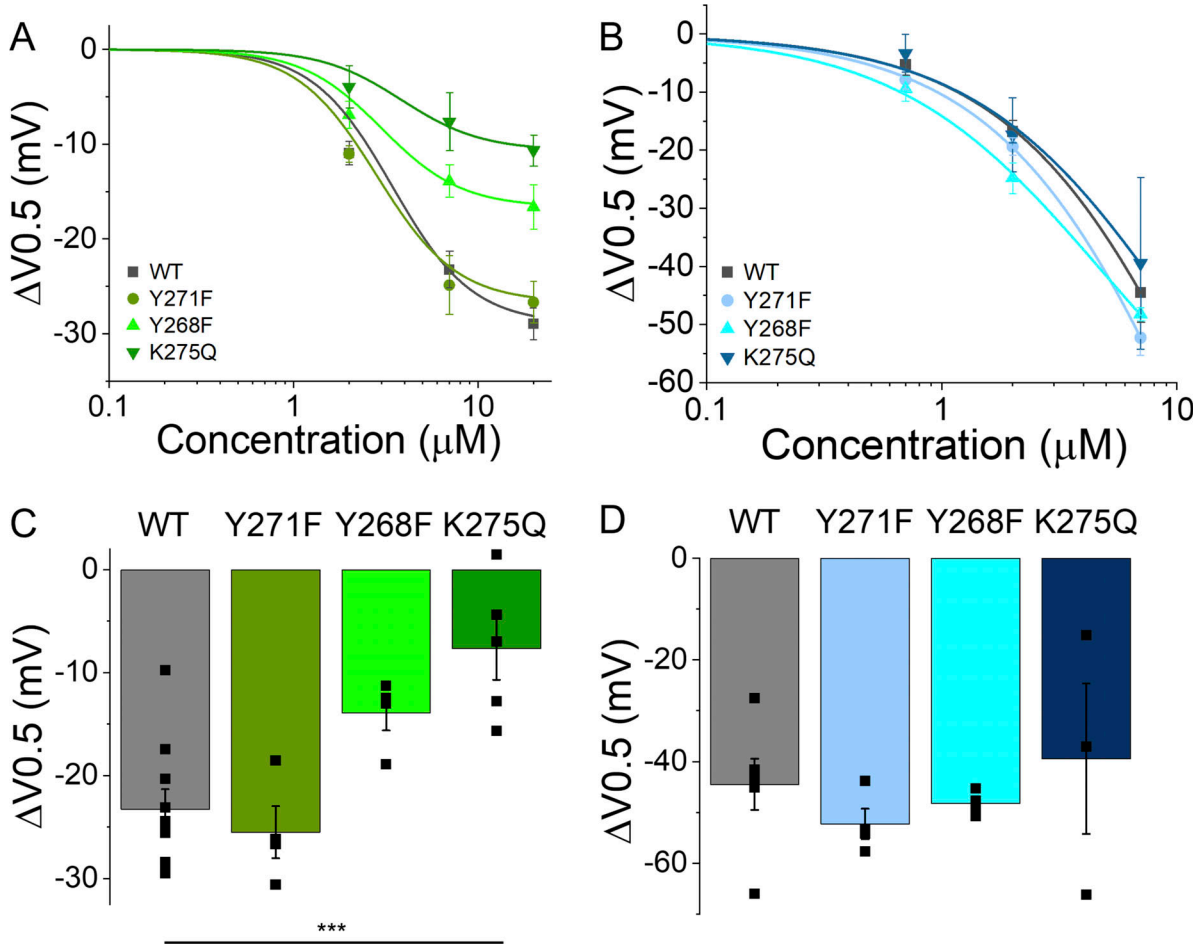

Figure 8. **Mutagenesis experiments show the importance of interacting residues from simulations.** Experiments were done on human KCNQ1 channel with the mutations Y281F, Y278F, and K285Q; the *Xenopus* numberings Y271F, Y268F, and K275Q were used here for ease of comparison with the simulations. **(A)** ΔV0.5 dose response curve of LIN-Gly on WT and point mutation KCNQ1 channels (WT n = 10, Y271F n = 3, Y268F n = 4, K275Q n = 5). **(B)** ΔV0.5 dose response curve of LIN-Tyr on WT and point mutation KCNQ1 channels (WT n = 6, Y271F n = 4, Y268F n = 4, K275Q n = 3). **(C)** Comparison of ΔV0.5 effect on WT KCNQ1 channels versus point mutations at 7 μM of LIN-Gly (WT: −25.28 ± 1.69 mV; n = 10, Y271F: −25.49 ± 2.53 mV; n = 3, Y268F: −13.91 ± 1.7 mV; n = 4, K275Q: −7.66 ± 3.04 mV; n = 5). ANOVA with Tukey's multiple comparison of WT to each point mutation gave ns for Y271F, P = 0.067 for Y268F and P = 0.0006 for K275Q. ***, P < 0.001. **(D)** Comparison of ΔV0.5 effect on WT KCNQ1 channels versus point mutations at 7 μM of LIN-Tyr (WT: −43.57 ± 1.03 mV; n = 3, Y271F: −52.28 ± 2.98 mV; n = 4, Y268F: −48.23 ± 1.15 mV; n = 4, K275Q: −39.47 ± 14.8 mV; n = 3). ANOVA with Tukey's multiple comparison of WT to each point mutation gave ns for all comparisons. Data shown as mean ± SEM.

region than Site I, so we suggest that the larger head groups of LIN-Gly and LIN-Tyr are detrimental to binding at Site II because they cannot fit into the small space of Site II. This inability for the larger PUFA analogs to fit into the small binding space could explain why LIN is able to interact with K316 more and thus has a larger G_{max} effect. We also see from our simulations that LIN-Tyr interacts more diffusely among residues in the Site II region than LIN-Gly, thus interacting less with the effector residues (i.e., K316; Fig. 6). This could explain why LIN-Tyr has even less of an effect than LIN-Gly on KCNQ1 G_{max}.

It is important to note that these studies are done in the KCNQ1 channel alone without the β subunit KCNE1. We use only the KCNQ1 channel in our simulations because the KCNQ1/KCNE1 complex structure has not yet been published. To test the validity of the simulations we therefore conducted our experiments on KCNQ1 alone. There are some differing effects of these same PUFAs on a KCNQ1/KCNE1 complex versus KCNQ1 alone, especially pertaining to Site II. For example, in contrast to this KCNQ1 data, previous studies of the KCNQ1/KCNE1 complex show that LIN-Gly increases the maximum conductance of the channel more than LIN (Bohannon et al., 2020b). However, many PUFA effects are similar in KCNQ1 and KCNQ1/KCNE1. For example, LIN-Gly has the same effects on the voltage dependence in KCNQ1 (this study) as it does in KCNQ1/KCNE1 (Bohannon et al., 2020b). While many PUFA effects are similar in KCNQ1 and KCNQ1/KCNE1, the differences in effects of G_{max} should still be considered when transferring the results of this study to the IKs channel. This difference in PUFA G_{max} effect on KCNQ1 and KCNQ1/KCNE1 could be due to that KCNE1 association with KCNQ1 causes a rotation of the voltage sensing domain. Cryo-EM has recently shown that when KCNE3 binds to KCNQ1, KCNE3 causes a 7° rotation of the voltage-sensing domain in KCNQ1 (Sun and Mackinnon, 2017). We have previously suggested that an even larger rotation occurs when KCNE1 binds

to KCNQ1 because KCNE1 is slightly wider than KCNE3 (Wu et al., 2021). PUFA binding Site II, which is responsible for the G_{max} effect, is located near the area of this conformational change. Thus, it is possible that when KCNE1 is bound, it allows for PUFAs to have a much larger G_{max} effect than when KCNE1 is not present.

In summary, in this study, we have found that the PUFA analogy LIN-Gly and LIN-Tyr have an improved ability to shift the voltage dependence over LIN via two different mechanisms. LIN-Gly has more simultaneous interactions at Site Iα (especially R221 and Y268), whereas LIN-Tyr binds only to Site Iβ. Since LIN-Tyr has the largest effect on shifting the voltage dependence, this indicates that Site Iβ is more effective than Site Iα. These simulations also suggest that LIN-Gly and LIN-Tyr interact less with the effector residues of Site II and more diffusely in this region, thereby having less of an effect on G_{max}. We propose that this is due to the larger size of their headgroups and the tight binding space of Site II. Overall, this study elucidates the mechanisms in which PUFA analogs better shift KCNQ1 voltage dependence and have decreased effects on G_{max}. These new understandings of the specific interactions these activators have with the KCNQ1 channel will help to guide drug development in this area. Drugs that improve KCNQ1 channel function could potentially be developed to treat LQT1.

Data availability

Simulations were carried out at the Pittsburg Supercomputing Center, which is funded by National Institute of General Medical Sciences. Data for all simulations are available at the following links:

https://doi.org/10.57971/pkpa-h928
https://commons.datacite.org/doi.org/10.57971/pkpa-h928
https://doi.org/10.57971/vtpb-d957
https://commons.datacite.org/doi.org/10.57971/vtpb-d957
https://doi.org/10.57971/2mn2-3m18
https://commons.datacite.org/doi.org/10.57971/2mn2-3m18
https://doi.org/10.57971/640a-gd68
https://commons.datacite.org/doi.org/10.57971/640a-gd68

Acknowledgments

Christopher J. Lingle served as editor.

Anton2 computer time was provided by the Pittsburgh Supercomputing Center through a grant from the National Institutes of Health (R01GM116961). The Anton2 machine at the Pittsburgh Supercomputing Center was generously made available by D.E. Shaw Research. This work was supported by the Swedish Society for Medical Research (to S.I. Liin), the Swedish Research Council (2017-02040, to S.I. Liin), the European Research Council under the European Union's Horizon 2020 research and innovation program (grant agreement No. 850622 to S.I. Liin), and the National Institutes of Health (R01HL131461, to H.P. Larsson).

Author contributions: J. Jowais, S. Yazdi, H.P. Larsson, and S.I. Liin contributed to study design and analysis approaches. S. Yazdi performed computational simulations. J. Jowais, V. Olivier-Meo, A. Golluscio, and S.I. Liin performed electrophysiological experiments. J. Jowais wrote the original draft. All authors commented on the manuscript and approved the final version.

Disclosures: S.I. Liin reported a patent number #62/032,739 pending. H.P. Larsson reported a patent to application (#62/032,739), including a description of the interaction of charged lipophilic compounds with the KCNQ1 channel, has been submitted by the University of Miami with H.P. Larsson and S.I. Liin identified as inventors, pending. In addition, H.P. Larsson is the equity owner of VentricPharm, a company that operates in the same field of research as the study. No other disclosures were reported.

Submitted: 12 January 2023
Revised: 2 May 2023
Accepted: 18 July 2023

References

Alders, M., H. Bikker, and I. Christiaans. 1993. Long QT syndrome. In GeneReviews((R)). M.P. Adam, H.H. Ardinger, R.A. Pagon, S.E. Wallace, L.J.H. Bean, G. Mirzaa, and A. Amemiya, editors. University of Washington. Seattle, WA. 3 pp.

Barhanin, J., F. Lesage, E. Guillemare, M. Fink, M. Lazdunski, and G. Romey. 1996. K(V)LQT1 and lsK (minK) proteins associate to form the I_{Ks} cardiac potassium current. *Nature*. 384:78–80. https://doi.org/10.1038/384078a0

Barro-Soria, R., S. Rebolledo, S.I. Liin, M.E. Perez, K.J. Sampson, R.S. Kass, and H.P. Larsson. 2014. KCNE1 divides the voltage sensor movement in KCNQ1/KCNE1 channels into two steps. *Nat. Commun.* 5:3750. https://doi.org/10.1038/ncomms4750

Bohannon, B.M., A. de la Cruz, X. Wu, J.J. Jowais, M.E. Perez, D.M. Dykxhoorn, S.I. Liin, and H.P. Larsson. 2020a. Polyunsaturated fatty acid analogues differentially affect cardiac Na_V, Ca_V, and K_V channels through unique mechanisms. *Elife*. 9:e51453. https://doi.org/10.7554/eLife.51453

Bohannon, B.M., X. Wu, X. Wu, M.E. Perez, S.I. Liin, and H.P. Larsson. 2020b. Polyunsaturated fatty acids produce a range of activators for heterogeneous IKs channel dysfunction. *J. Gen. Physiol.* 152:e201912396. https://doi.org/10.1085/jgp.201912396

Bohnen, M.S., G. Peng, S.H. Robey, C. Terrenoire, V. Iyer, K.J. Sampson, and R.S. Kass. 2017. Molecular pathophysiology of congenital long QT syndrome. *Physiol. Rev.* 97:89–134. https://doi.org/10.1152/physrev.00008.2016

Cho, Y. 2016. Management of patients with long QT syndrome. *Korean Circ. J.* 46:747–752. https://doi.org/10.4070/kcj.2016.46.6.747

Chockalingam, P., L. Crotti, G. Girardengo, J.N. Johnson, K.M. Harris, J.F. van der Heijden, R.N. Hauer, B.M. Beckmann, C. Spazzolini, R. Rordorf, et al. 2012. Not all beta-blockers are equal in the management of long QT syndrome types 1 and 2: Higher recurrence of events under metoprolol. *J. Am. Coll. Cardiol.* 60:2092–2099. https://doi.org/10.1016/j.jacc.2012.07.046

Colquhoun, D., A.G. Hawkes, and K. Srodzinski. 1996. Joint distributions of apparent open and shut times of single-ion channels and maximum likelihood fitting of mechanisms. *Philos. Trans. Royal Soc.* 354:2555–2590. https://doi.org/10.1098/rsta.1996.0115

Daura, X., W.F. van Gunsteren, and A.E. Mark. 1999. Folding-unfolding thermodynamics of a β-heptapeptide from equilibrium simulations. *Proteins*. 34:269–280. https://doi.org/10.1002/(SICI)1097-0134(19990215)34:3<269::AID-PROT1>3.0.CO;2-3

Hou, P., J. Eldstrom, J. Shi, L. Zhong, K. McFarland, Y. Gao, D. Fedida, and J. Cui. 2017. Inactivation of KCNQ1 potassium channels reveals dynamic

coupling between voltage sensing and pore opening. *Nat. Commun.* 8: 1730. https://doi.org/10.1038/s41467-017-01911-8

Klauda, J.B., V. Monje, T. Kim, and W. Im. 2012. Improving the CHARMM force field for polyunsaturated fatty acid chains. *J. Phys. Chem. B.* 116: 9424–9431. https://doi.org/10.1021/jp304056p

Liin, S.I., J.E. Larsson, R. Barro-Soria, B.H. Bentzen, and H.P. Larsson. 2016. Fatty acid analogue N-arachidonoyl taurine restores function of I_{Ks} channels with diverse long QT mutations. *Elife.* 5:e20272. https://doi.org/10.7554/eLife.20272

Liin, S.I., M. Silverå Ejneby, R. Barro-Soria, M.A. Skarsfeldt, J.E. Larsson, F. Starck Härlin, T. Parkkari, B.H. Bentzen, N. Schmitt, H.P. Larsson, et al. 2015. Polyunsaturated fatty acid analogs act antiarrhythmically on the cardiac I_{Ks} channel. *Proc. Natl. Acad. Sci. USA.* 112:5714–5719. https://doi.org/10.1073/pnas.1503488112

Liin, S.I., S. Yazdi, R. Ramentol, R. Barro-Soria, and H.P. Larsson. 2018. Mechanisms underlying the dual effect of polyunsaturated fatty acid analogs on Kv7.1. *Cell Rep.* 24:2908–2918. https://doi.org/10.1016/j.celrep.2018.08.031

Lippert, R.A., C. Predescu, D.J. Ierardi, K.M. Mackenzie, M.P. Eastwood, R.O. Dror, and D.E. Shaw. 2013. Accurate and efficient integration for molecular dynamics simulations at constant temperature and pressure. *J. Chem. Phys.* 139:164106. https://doi.org/10.1063/1.4825247

Marrink, S.J., V. Corradi, P.C.T. Souza, H.I. Ingólfsson, D.P. Tieleman, and M.S.P. Sansom. 2019. Computational modeling of realistic cell membranes. *Chem. Rev.* 119:6184–6226. https://doi.org/10.1021/acs.chemrev.8b00460

Martyna, G.J. 1994. Remarks on "Constant-temperature molecular dynamics with momentum conservation". *Phys. Rev. E Stat. Phys. Plasmas Fluids Relat. Interdiscip. Top.* 50:3234–3236. https://doi.org/10.1103/physreve.50.3234

Noskov, S.Y., and B. Roux. 2008. Control of ion selectivity in LeuT: Two Na^+ binding sites with two different mechanisms. *J. Mol. Biol.* 377:804–818. https://doi.org/10.1016/j.jmb.2008.01.015

Salata, J.J., N.K. Jurkiewicz, B. Jow, K. Folander, P.J. Guinosso Jr, B. Raynor, R. Swanson, and B. Fermini. 1996. Ik of rabbit ventricle is composed of two currents: Evidence for IKs. *Am. J. Physiol.* 271:H2477–H2489. https://doi.org/10.1152/ajpheart.1996.271.6.H2477

Sanguinetti, M.C., M.E. Curran, A. Zou, J. Shen, P.S. Spector, D.L. Atkinson, and M.T. Keating. 1996. Coassembly of K_VLQT1 and minK (IsK) proteins to form cardiac I_{Ks} potassium channel. *Nature.* 384:80–83. https://doi.org/10.1038/384080a0

Schwartz, P.J., L. Crotti, and R. Insolia. 2012. Long-QT syndrome: From genetics to management. *Circ. Arrhythm. Electrophysiol.* 5:868–877. https://doi.org/10.1161/CIRCEP.111.962019

Sun, J., and R. MacKinnon. 2017. Cryo-EM structure of a KCNQ1/CaM complex reveals insights into congenital long QT syndrome. *Cell.* 169: 1042–1050.e9. https://doi.org/10.1016/j.cell.2017.05.019

Sun, J., and R. MacKinnon. 2020. Structural basis of human KCNQ1 modulation and gating. *Cell.* 180:340–347.e9. https://doi.org/10.1016/j.cell.2019.12.003

Tuckerman, L.S., and J. Bechhoefer. 1992. Dynamical mechanism for the formation of metastable phases: The case of two nonconserved order parameters. *Phys. Rev. A.* 46:3178–3192. https://doi.org/10.1103/physreva.46.3178

Waddell-Smith, K.E., J.R. Skinner, and members of the CSANZ Genetics Council Writing Group. 2016. Update on the diagnosis and management of familial long QT syndrome. *Heart Lung Circ.* 25:769–776. https://doi.org/10.1016/j.hlc.2016.01.020

Westhoff, M., J. Eldstrom, C.I. Murray, E. Thompson, and D. Fedida. 2019. IKs ion-channel pore conductance can result from individual voltage sensor movements. *Proc. Natl. Acad. Sci. USA.* 116:7879–7888. https://doi.org/10.1073/pnas.1811623116

Wu, X., M.E. Perez, S.Y. Noskov, and H.P. Larsson. 2021. A general mechanism of KCNE1 modulation of KCNQ1 channels involving non-canonical VSD-PD coupling. *Commun. Biol.* 4:887. https://doi.org/10.1038/s42003-021-02418-1

Yazdi, S., J. Nikesjö, W. Miranda, V. Corradi, D.P. Tieleman, S.Y. Noskov, H.P. Larsson, and S.I. Liin. 2021. Identification of PUFA interaction sites on the cardiac potassium channel KCNQ1. *J. Gen. Physiol.* 153:e202012850. https://doi.org/10.1085/jgp.202012850

Supplemental material

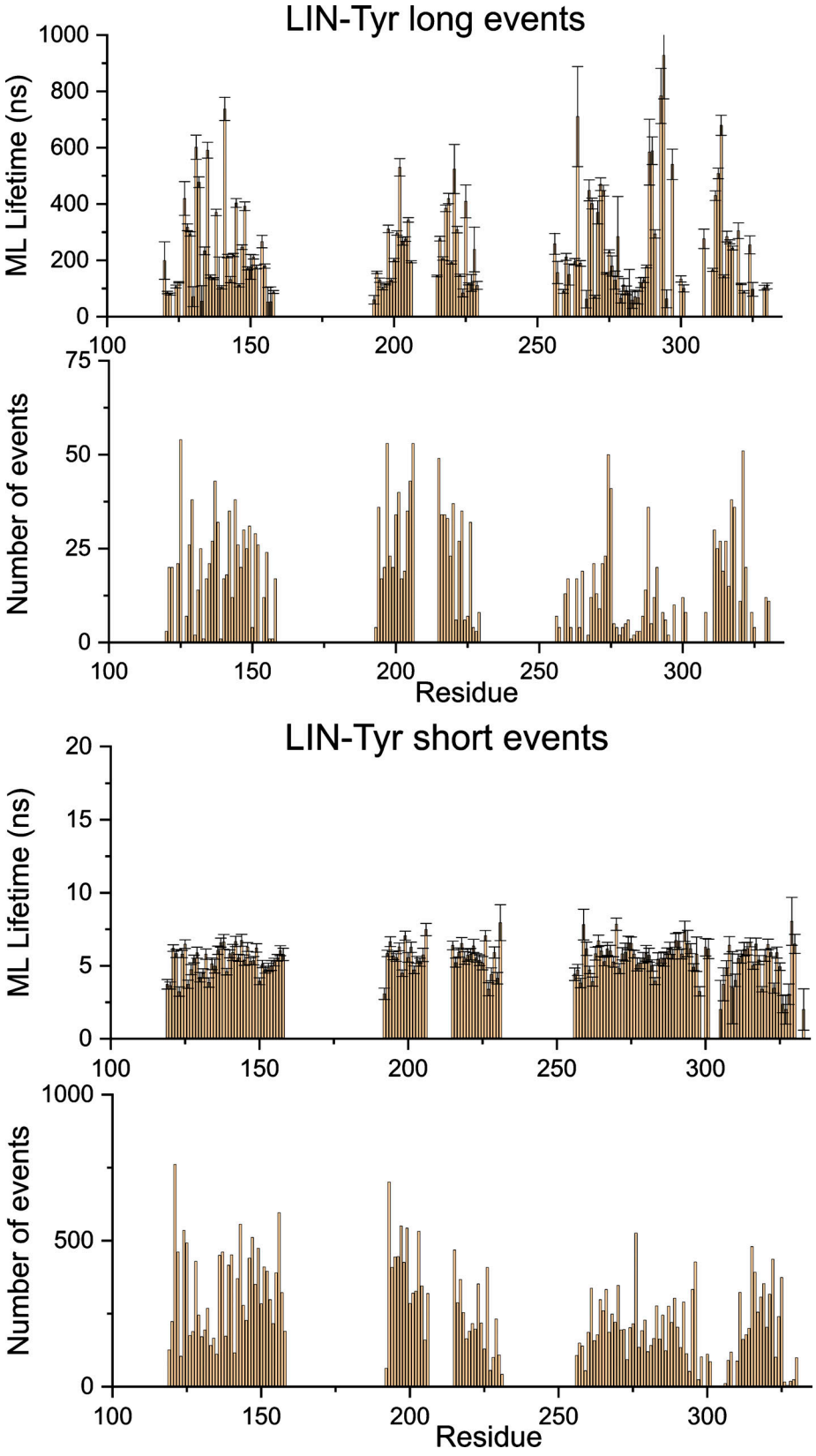

Figure S1. **Most likely lifetimes of LIN-Tyr interactions from Maximum-Likelihood fits.** Most likely lifetimes of (top) long interaction events and (bottom) short interaction events for LIN-Tyr for each residue calculated from data of both the LIN-Tyr Site I and Site II simulations (Fig. 3). The starting configuration (i.e., a LIN-Tyr in Site I or Site II) had little effect of the distributions (see Fig. 3) as a number of LIN-Tyr molecules bind and unbind from the different residues. Therefore, the interaction events from the two simulations were combined to increase the number of events for better statistics. The total number of events in each case is also shown. Data given as mean ± SD.

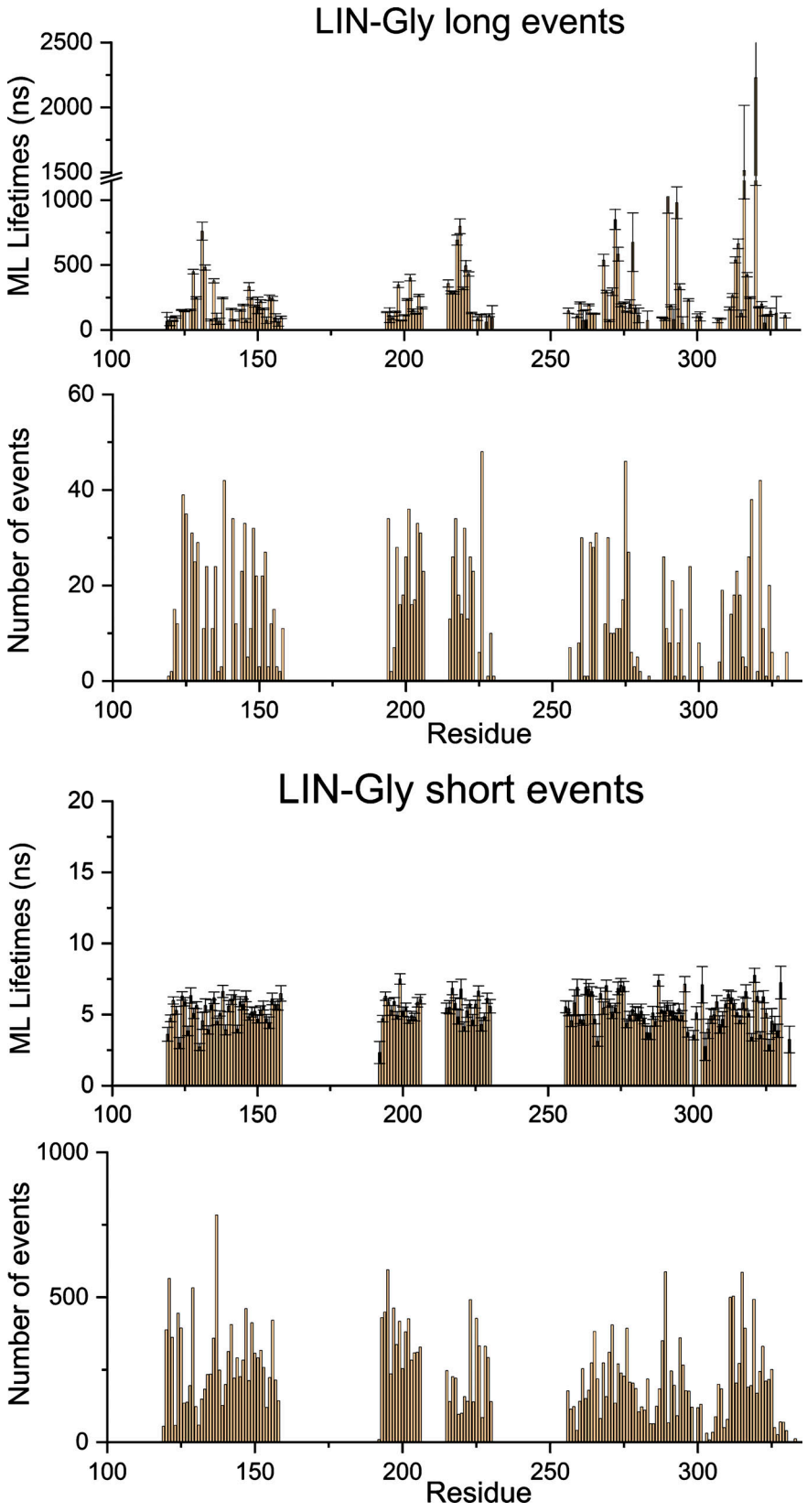

Figure S2. **Most likely lifetimes of LIN-Gly interactions from Maximum-Likelihood fits.** Most likely lifetimes of (top) long interaction events and (bottom) short interaction events for LIN-Gly for each residue calculated from data of both the LIN-Gly Site I and Site II simulations (Fig. 3). The starting configuration (i.e., a LIN-Gly in Site I or Site II) had little effect of the distributions (see Fig. 3) as a number of LIN-Gly molecules bind and unbind from the different residues. Therefore, the interaction events from the two simulations were combined to increase the number of events for better statistics. The total number of events in each case is also shown. Data given as mean ± SD.